Observations on muon multiplicity distribution with the GRAPES-2 experiment at Ooty for studies on the mass composition of cosmic rays at PeV energies

S. K. Gupta,* N. V. Gopalakrishnan, A. V. John, D. K. Mohanty, S. D. Morris, K. C. Ravindran, K. Sivaprasad, B. V. Sreekantan, R. Srivatsan, and S. C. Tonwar
Tata Institute of Fundamental Research, Mumbai 400005, India
(Received 22 May 2003; published 29 September 2003)

Precise knowledge of the mass composition of the primary cosmic ray flux below and above the knee in the primary energy spectrum at $E \sim 3 \times 10^{15}$ eV is essential for understanding the acceleration and propagation of high energy cosmic rays. Simulations have shown that the correlations between the electron and muon components of showers are very sensitive to the mass of the primary nuclei. In particular, different regions of the muon multiplicity distribution observed with a large area muon detector, for well-defined selection on the electron component of showers, have a high sensitivity to different nuclear groups present in the primary flux. The GRAPES-2 experiment at Ooty seeks to exploit this sensitivity using a 200 m^2 area muon detector to study the mass composition of the primary flux in the energy range 10^{14}–10^{16} eV. The details of the experiment are presented and early observations are discussed in relation to the expectations from simulations.

DOI: 10.1103/PhysRevD.68.052005 PACS number(s): 96.40.De, 13.85.Tp, 96.40.Pq

I. INTRODUCTION

The origin of high energy ($\geqslant 10^{12}$ eV) cosmic rays [1] has remained an unresolved problem in astrophysics for a long time, although considerable progress [2,3] has been achieved in recent times. There are two broad scenarios for addressing the problem of the origin of cosmic rays. In the first and more direct scenario, the directional distribution of neutral cosmic radiation, viz., γ rays, has been studied to provide the identity of potential sources. However, observations [4,5] have shown the flux of γ rays to be very small, $\leqslant 0.1\%$ of the total cosmic ray particle flux. Further, it is very difficult to identify showers initiated by primary γ rays in the presence of the huge background of showers due to charged cosmic rays. Therefore, presently, detailed studies of the charged component of cosmic rays offer the only means to understand the astrophysics of high energy cosmic rays.

At energies above 10^{14} eV the flux of cosmic rays is too small to be detected by satellite or balloon borne detectors flying above the atmosphere due to constraints on achieving very large exposure factors with moderately heavy payloads. Although the energy spectra for various nuclear groups have been well measured with detectors flown aboard long-flying balloons [6,7] at energies around $\sim 10^{12}$ eV, the statistics at energies above 10^{13} eV are inadequate to extrapolate the measured spectra to the energy of the knee [8]. Therefore, measurements on the energy spectra of various nuclear groups at energies above $\sim 10^{14}$ eV have to rely presently on indirect observations of the products of interactions of primary cosmic ray particles in the atmosphere.

A high energy, $E_o \geqslant 10^{14}$ eV, primary cosmic ray particle incident on the top of the atmosphere creates a shower of particles through successive interactions, which is called an extensive air shower (EAS). The particles in the shower spread out laterally as they move downward due to the transverse momenta acquired at production. Detectable shower products may be classified into four distinct components: namely, the electron component ($e^{\pm}$ and γ rays), the muon component ($\mu^{\pm}$), the hadron component (pions, kaons, nucleons, etc.), and Cherenkov photons. The characteristics of these components depend on the energy and the mass of the primary cosmic ray particle in a complex way, and it is necessary to optimize the observable parameters, based on detailed simulations of the development of showers in the atmosphere. It is now well recognized that the muon component has the highest sensitivity for distinguishing between various primary nuclei due to a combination of several factors, namely, the slow (logarithmic) energy dependence of secondary pion production and the fact that a shower initiated by a nucleus with A nucleons and energy E_o can be considered, to a good approximation, to be a superposition of A showers, each initiated by a nucleon of energy E_o/A.

Most of the early experiments [9] have studied the muon component associated with air showers with relatively small area detectors, usually a few tens of m^2 for lower energies observed on the ground and only a few m^2 for higher energies deeper underground. It was only in the last few years that several groups, e.g., EAS-TOP [10], CASA-MIA [11], KASCADE [12], GAMMA [13], GRAPES-2 [14], and GRAPES-3 [15], have reported results on primary cosmic ray composition from observations with large area muon detectors with threshold energies ~GeV in association with air showers using somewhat different analysis procedures. Several groups, e.g., MACRO [16], Soudan-2 [17], KGF [18], BAKSAN [19], DELPHI(LEP) [20], and ALEPH(LEP) [21] have also reported observations on multiplicity distributions for very high energy muons observed with large area detectors placed deep underground. There are also reports on correlated observations on high energy muons with MACRO [22] and LVD [23] in association with showers observed with the EAS-TOP array. Similarly, preliminary results on the energy spectrum and multiplicity distribution for high energy muons have also been reported by the L3+C group

*Electronic address: guptask@tifr.res.in

[24] from observations with the L3 muon spectrometer located 30 m underground and a small air shower array on the surface. Measurements on the primary energy spectrum and composition using other components of air showers have been reviewed by Sommers [3] recently.

Detailed Monte Carlo simulations show that measurements on the distribution of the number of muons incident over a large area detector, usually called the muon multiplicity distribution, along with good measurements on the electron component of showers accompanying the muons, offer a very promising means to study the energy dependence of the composition of primary flux at energies above 10^{14} eV. The Gamma Ray Astronomy at PeV EnergieS Phase 2 (GRAPES-2) experiment has been designed with this objective in mind. As the name implies, a major thrust of the experiment designed in the late 1980s was to search for directional excess among ''μ-poor'' showers to optimize the detection of discrete sources of ultrahigh energy γ rays. The GRAPES-2 experiment is a natural follow-up of the successful GRAPES-1 experiment (1984–1987) which yielded some episodic detections [25–29] of several x-ray binaries, such as Cygnus X-3, Hercules X-1, Scorpius X-1, etc. The GRAPES-2 experiment is located at Ooty (11.4°N latitude, 76.3°E longitude and 2200 m altitude), a popular mountain resort town in southern India.

In the next section, we present the salient features of the GRAPES-2 experimental system. In Sec. III some of the basic results from relatively simple Monte Carlo simulations are presented, which show that different regions of the muon multiplicity distribution, obtained for showers selected with well-defined criteria for the electron component, have significant sensitivity for different primary nuclear groups. These results reveal the importance of observations with a large area muon detector with modular design. Some of the observational results are discussed in Sec. IV along with expectations from simulations. Finally, Sec. V presents the summary and the prospects.

II. GRAPES-2 EXPERIMENTAL SYSTEM

The EAS array for the GRAPES-2 experiment consists of 100 unshielded ''electron'' detectors and a 192-module 200 m^2 area shielded ''muon'' detector. The layout of the detectors is shown schematically in Fig. 1. The signals from the electron detectors are used to measure particle densities and arrival times in an EAS. Due to the limitations imposed by the ground topography around the laboratory building, the placement of electron detectors, with inter-detector spacing of $\sim$10 m, is hexagonally symmetric only up to about 40 m from the center, that is, for 61 detectors placed within the inner four rings. However, the outer detectors 62–85 provide a good sampling of particle density for core distances up to $\sim$80 m for showers whose cores are located within $\sim$30 m of the array center. The interdetector separation of only 10 m for the GRAPES-2 array makes it one of the most compact arrays in the world, leading to a relatively lower energy detection threshold and more accurate reconstruction of shower characteristics including the arrival direction.

The center of the large (200 m^2) area muon detector is

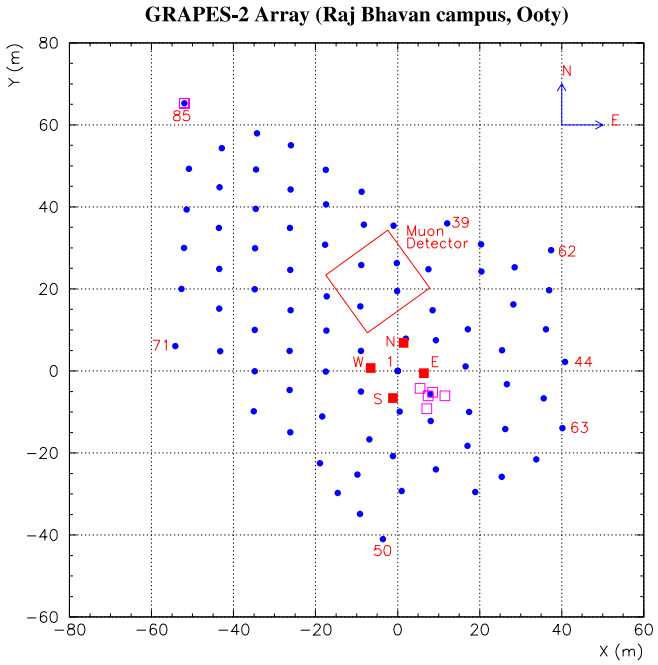

FIG. 1. Layout of the electron and muon detectors for the GRAPES-2 shower array.

located at a distance of $\sim$25 m from the array center and the distance of individual muon detector modules from the array center varies from 15 to 40 m. A total of 16 tunnels, each 21 m deep, were made by digging into the hillside to accommodate the 192 muon detector modules. The physical layout for the muon detector modules, the tunnels, and the absorber is shown schematically in Fig. 2. The tunnels are covered by a 0.3 m thick reinforced concrete slab, which takes the load of a 3.5 m thick layer of packed soil placed above it and provides an overburden of 600 g cm^{-2}, which sets the energy threshold of 1 GeV for vertical muons.

A. Electron detectors

Most of the electron detectors consist of plastic scintillators, 100 cm $\times$ 100 cm in area and 5 cm thick, placed inside an aluminum tank and viewed by a fast 2 in. photomultiplier tube (PMT) from a height of 65 cm. Studies with a prototype detector have shown that this resulted in a variation of $\sim$10% in the signal from the center to the corner of the detector. A special feature of the GRAPES-2 array, relevant for the observations discussed here, is the use of four special

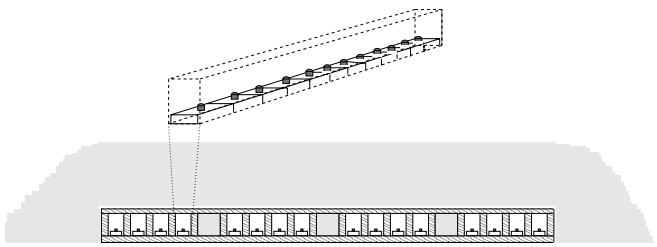

FIG. 2. Schematic layout of the 16 tunnels housing the muon detectors and the absorber shielding these detectors.

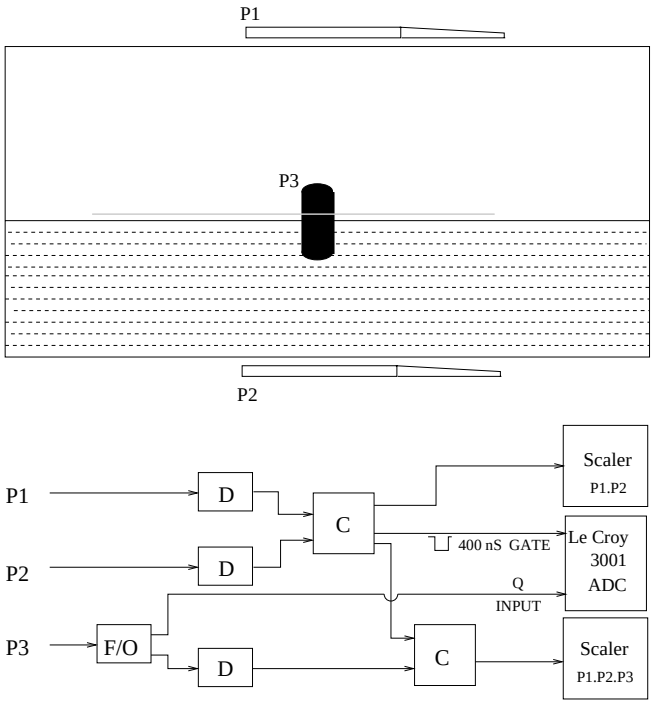

FIG. 3. Schematic sketch of the prototype water Cherenkov detector module and the trigger detectors used for optimizing the design features.

purpose liquid scintillation detectors called north (N), east (E), west (W), and south (S), located on the corners of a square of side ~ 9 m around the array center, which are being used for generating the fourfold shower trigger (NEWS). Each of these four detectors uses a 10 cm deep column of mineral oil based organic liquid scintillator inside an aluminum tank of 80 cm$\times$ 80 cm.

B. Muon detectors

The design of the muon detector modules in the GRAPES-2 array was based on the following four criteria; fast response (~ 5 ns), high efficiency ($\geqslant 95\%$), reliable and safe long-term operation, and low cost. The motivation for having fast response was to provide the option to trigger on muons in the EAS. Studies [30] carried out with a prototype water Cherenkov detector (WCD) demonstrated its suitability for use as a muon detector that is fast, efficient, safe, and economical.

The prototype WCD module, shown in Fig. 3, consisted of an aluminum tank 170 cm$\times$61 cm$\times$80 cm in size. The rectangular dimensions of the module were dictated by the design of the long narrow tunnels (Fig. 2). A fast PMT (ETL 9807B) was suspended from the top cover of the tank. The front face of the PMT was dipped in water to a depth of ~ 1 cm for efficient collection of Cherenkov photons. In addition, a secondary cover, also made from a thin aluminum sheet, was suspended inside the tank just above the water level to simulate a water tank of variable height.

The response of the prototype WCD module to throughgoing muons has been studied using a muon trigger generated by a twofold coincidence between signals from two

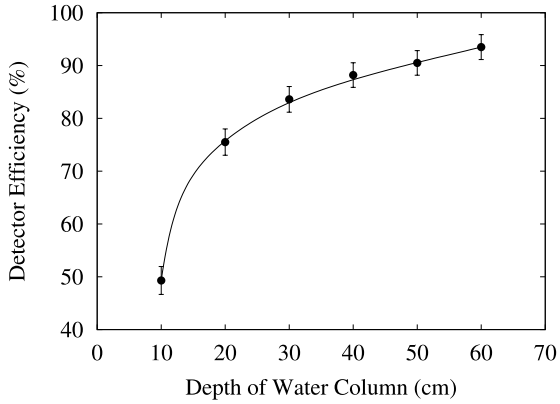

FIG. 4. Variation of the muon detection efficiency of the prototype WCD as a function of the depth of water column for pure distilled water. The curve represents only an eye-fit.

plastic scintillator pedals P_1 and P_2 placed above and below the aluminum tank, respectively, as shown in Fig. 3. The pulse $P_1.P_2$ is applied as the GATE to a charge-integrating input of the multichannel analyzer (MCA, LeCroy QVT model 3001). The anode pulse from the PMT, P_3, viewing the water, is connected to the *Q* input of the MCA after suitable delay. The ratio of the number of threefold ($P_1.P_2.P_3$) to twofold ($P_1.P_2$) coincidences is used for measuring the muon detection efficiency of the WCD module. The ratio of the mean charge of MCA distributions for two different heights of the water column equals the ratio of the number of photons detected for the corresponding heights of the water column. Note that a relativistic ($\beta \sim 1$) charged particle emits Cherenkov photons in water along a cone of half angle $\sim 41°$ and the number of photons emitted per unit path length is given by the standard relation

$$\frac{dN}{dX} = 2\pi\alpha \sin^2\theta\left(\frac{1}{\lambda_1} - \frac{1}{\lambda_2}\right), \tag{1}$$

where $\alpha = 1/137$ is the fine structure constant, $\theta = 41.4°$ for ultrarelativistic particles, and λ_1 and λ_2 are the minimum and maximum wavelengths, respectively, of the emitted Cherenkov photons. For the wavelength range of 300–500 nm, the number of Cherenkov photons emitted is ~ 270 cm^{-1}.

The variation of the muon detection efficiency of the prototype WCD module with the height of the water column is shown in Fig. 4 as the height is increased from 10 cm to 60 cm. The efficiency increases with column height, reaching a maximum of $\sim 95\%$ at 60 cm. The variation of the mean charge of the pulse from the prototype WCD module as a function of the height of the water column is shown in Fig. 5, which shows that the response of the WCD is linear with the height of the water column.

Since the Cherenkov emission is predominantly in the ultraviolet, it is rapidly absorbed in water, resulting in significant loss of signal. To increase the yield of detectable photons, it was decided to use a wavelength shifter dye, β-methyl umbelliferone, which readily dissolves in a mildly alkaline solution of sodium hydroxide in water. This dye is

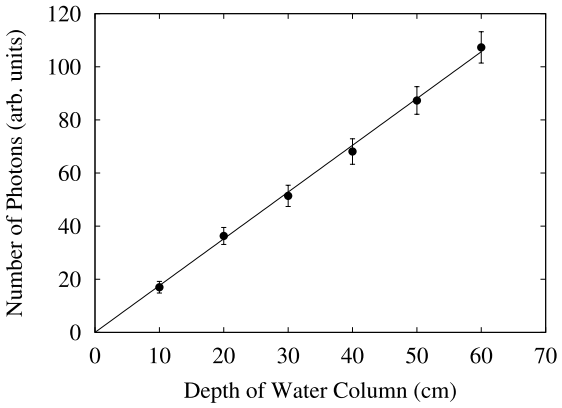

FIG. 5. Variation of the mean pulse amplitude from the prototype WCD as a function of the depth of water column for distilled water.

known [31] to absorb photons over the wavelength range 300–380 nm, with a broad peak at 320 nm, and reemit photons over the range 400–500 nm, with a peak at 440 nm. Since the aluminum container for the prototype WCD precluded the use of sodium hydroxide solution, an attempt was made to dissolve the dye in pure distilled water. The dye dissolved satisfactorily after vigorous stirring of the mixture for several hours with motorized stainless steel rotors. Subsequent long-term observations have established that the dye has stayed dissolved even after a span of several years.

Measurements have also been made to determine the optimum dye concentration for the prototype design of the WCD. The observed variation of the muon detection efficiency as a function of the dye concentration for a 20 cm deep water tank is shown in Fig. 6. It is seen that the efficiency starts to saturate at $\sim$95% at a dye concentration of 10^{-3} g/l. Based on the results discussed above, it was decided to use aluminum tanks 170 cm$\times$61 cm $\times$25 cm in size, filled with a dilute (2×10^{-3} g/l) solution of β-methyl umbelliferone in distilled water to a depth of 20 cm.

Observations with the first few tanks spread over several months revealed that the presence of water vapor around the

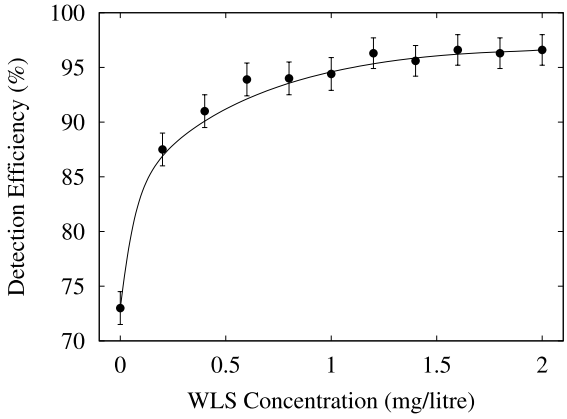

FIG. 6. Variation of the muon detection efficiency of the prototype WCD as a function of the concentration of the dye (β-methyl umbelliferone) dissolved in distilled water. The curve represents only an eye fit.

base of the PMT was causing corrosion on the PMT pins, leading to gradual loss in gain and finally evaporation of the photocathode. Therefore a sealed container was designed for the PMT and its base. The container also ensured good optical contact between the photocathode and the water in the tank. Optical coupling between the photocathode and the front part of the glass container is obtained by filling the gap between the PMT face and the inside face of the glass container with clear silicone oil having nearly the same refractive index as the PMT face.

As expected for the rectangular (170 cm$\times$61 cm) design of the water tank, the response of the detector is not uniform over its surface area. Detailed measurements were made to study the response of the detector as a function of the location of muons on its surface [32]. Observations showed that the mean amplitude of the signal from the PMT for muons going near the center of the tank was 2.1 times the mean for muons going near the corners of the tank. This result was satisfactorily understood through relatively simple Monte Carlo simulations which took into consideration the tank geometry, the reflectivity of the inner surfaces, the spectrum of Cherenkov photons, the wavelength shifting of photons due to β-methyl umbelliferone, and the quantum response of the PMT. With simple approximations about various processes taking place inside the tank, the simulations predicted the ratio of the mean amplitude from the central region to be 1.7 times larger than that for muons going near the corners. In view of various simplifying assumptions underlying the simulations, the agreement between the observed (2.1) and the expected (1.7) ratios is considered to be reasonable. Also, this large value of the ratio is not a matter of concern since the response of the WCD module is proposed to be used to generate a YES/NO signal for one or more muons passing through it in association with air showers, as mentioned earlier.

C. Signal processing and shower selection

Figure 7 shows a block diagram of the electronics used to process the signals from the electron and muon detectors. The anode signal from the photomultiplier of each of the electron detectors is split into two parts, in the ratio of 0.8:0.2. The smaller (0.2) signal is digitized using charge-integrating analog-to-digital converters ADCs (LeCroy 2249A) after suitable cable delay. The larger (0.8) signal is amplified (gain 10) and discriminated and fed to time-to-digital converters (TDCs, LeCroy 2228A). The anode signal from each of the muon detector modules is amplified (gain 10), discriminated, and latched in the 192-bit muon detector latch (MDL) system.

Figure 7 also shows the logic used for selection of showers and generation of the shower trigger which initiates the readout of the data acquisition system. As mentioned above, a special feature of the GRAPES-2 experiment is the requirement for the core of most of the selected showers to lie in the central area of the array. For this purpose, a fourfold coincidence between signals from each of the four centrally placed detectors N, E, W and S is required for generating a shower trigger. Each of the NEWS detectors is required to be larger

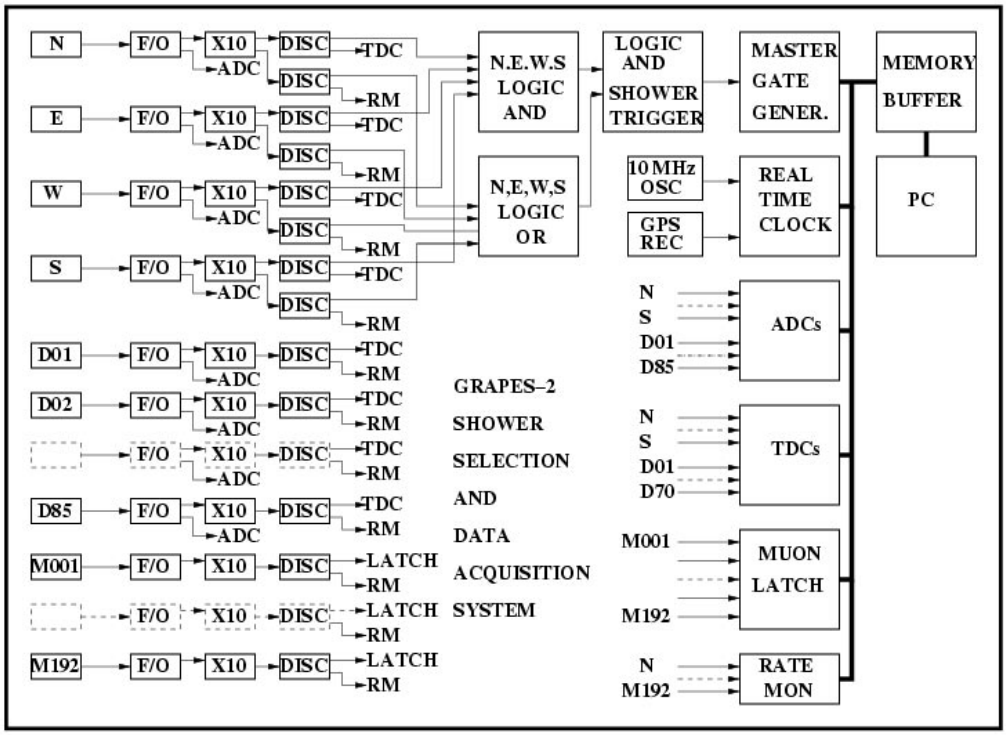

FIG. 7. Block diagram of the electronics used for processing of the anode signals from the electron and muon detectors. Also shown are the data acquisition and recording system.

than ~ 0.3 times the signal I^{min} for a minimum ionizing particle (MIP) through the detector. However, the trigger has been designed to disfavor the selection of very small showers by imposing the additional requirement that one of the NEWS detectors should have a signal larger than $\geqslant 3$ MIPs. The mean rate of the shower trigger has been observed to be 5.9 per minute.

D. Data acquisition system and data recording

The NEWS trigger serves as the GATE/START for initiating the conversion process in the ADCs and TDCs, after passing through a module (MASTER) which controls the data readout sequence and prevents the generation of another trigger during the data readout. In addition, two more triggers, the pedestal (PED) and global positioning system (GPS) are connected to the MASTER module. The PED trigger (0.1 Hz) is generated by a local oscillator to record ADC pedestals. The GPS trigger is the ''minute'' signal from the GPS module (Meinberg 167BGT) which is used as the time marker for the real time clock (RTC) which is run on an independent temperature-stabilized (~ 1 part in 10^8) quartz crystal oscillator (Oscilloquartz OSC22). The RTC is latched by each shower trigger, allowing the absolute time of each trigger to be recorded to an accuracy of 10 μs. Similarly, the start gate from the MASTER module latches the 192-bit output of MDL to record the number of muon detectors triggered.

Figure 7 also shows the block diagram of the data acquisition system used for the GRAPES-2 experiment. In addition to the nine ADC modules (108 channels) and 13 TDC modules (104 channels) used for recording the pulse amplitude and timing information for the electron detectors, the 64-bit output of the RTC and the 192-bit output of the muon detector is also recorded as 8-bit bytes. In addition, some housekeeping information such as the serially generated event number, trigger identification bits, and event start identification bits are also recorded for each trigger. Following a readout trigger from the MASTER module, the data are transferred from various data modules (ADCs, TDCs, RTC, MDL, etc.) to one of the 32 kbyte dual memory buffers using a 1 MHz clock. When full, the contents of each buffer are read out by an Intel processor with a safe handshake protocol and stored on the hard disk. With the use of intermediate memory buffers, the dead time of the system was limited to less than 0.5 ms, which allowed the possibility of recording possible short-duration shower bursts.

E. Detector calibrations and monitoring

The electron detectors are calibrated routinely twice a month using through-going muons. This value is used later during analysis to convert ADC counts for shower triggers to obtain the equivalent number of MIPS in the electron detectors. The muon detectors are also calibrated routinely in a similar manner but only the muon detection efficiency is

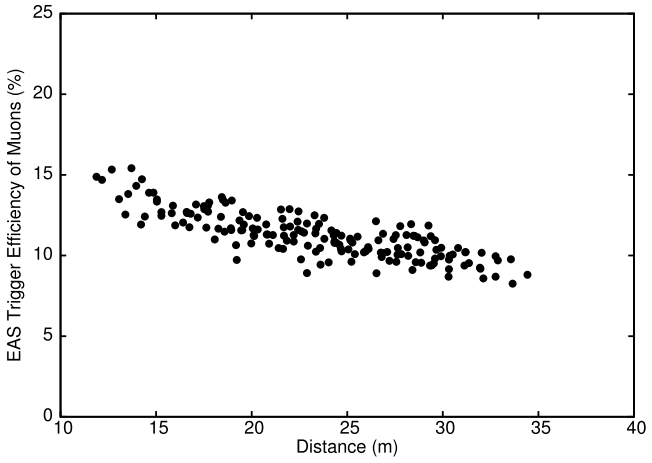

FIG. 8. Distribution of the 'EAS trigger' efficiency of the muon detector module as a function of the distance of the module from the array center.

measured. It is ensured that the muon detection efficiency for all the modules is $\sim 95\%$ at all times. However, if this value for any module falls significantly below 95%, the module is treated as nonworking and suitable repairs are initiated.

The performance of both electron and muon detectors is also monitored continuously using on-line software through measurement of EAS trigger efficiencies. For the electron detectors, the ratio of the number of showers having $\geqslant 3$ MIPS in each detector to the total number of showers is the quantity that is monitored for constancy in addition to the constancy of the shower trigger (NEWS) rate itself. For each muon detector module, the ratio of the number of showers showing the YES signal to the total number of showers is monitored.

Since the shower trigger has been designed to preferentially select small showers with their cores near the center of the array, it is interesting to observe the reflection of the lateral distribution of muons in the distribution (Fig. 8) of EAS trigger efficiency as a function of the distance of the muon detector module from the array center. Assuming Poisson distribution, a value of 0.10 for the trigger efficiency corresponds to an average muon density of ~ 0.10 at a distance of about 30 m from the array center. Using the lateral distribution of muons, discussed later in Sec. III A, the average muon size (N_μ) of showers can be estimated to be ~ 7500. Since most of the shower triggers are generated by proton primaries, particularly close to the threshold, this value of N_μ corresponds to an average shower size of $\sim 4.2\times 10^5$ for near vertical showers with average primary proton energy $\sim 10^{15}$ eV.

III. MUON MULTIPLICITY DISTRIBUTIONS

The muon multiplicity distribution (MMD) has been used by several groups [16–23] for studies on the composition of primary cosmic ray flux. However, observations of the muon component, without any constraints from the electron component, are dominated by protons, with different ranges of muon numbers being contributed mainly by protons of different energies. A selection on the associated electron component reduces the contribution of dominant low energy protons and enhances the sensitivity to the heavier nuclei in the primary flux.

These important features of the MMD, for showers of well-defined electron component, were seen from relatively simple Monte Carlo simulations. It is important to note here that the basic features of the MMD are the result of the ''average'' development of showers in the atmosphere and large but relatively rare fluctuations contribute very little to these basic features. Therefore, we have adopted here a semi Monte Carlo simulation technique for studying broad features of the MMD for a few possible models for energy spectra of various nuclear components in the primary flux. We have assumed the primary flux to be composed of five nuclear groups, namely, protons (mass number $A=1$), helium ($A=4$), the CNO group ($A=14$), the silicon group ($A=28$), and the iron group ($A=56$). In addition, we have anchored the energy spectra of these groups to flux values at a total energy of 1 TeV as given by the parametrization of data from direct measurements [33]. In order to account for the knee at energies $E\sim 3\times 10^{15}$ eV, it has been assumed that the energy spectrum for each of the five components becomes steeper by 0.5 in the power law spectral exponent at a ''rigidity cutoff'' value of $Z/A\times E_c$, where Z is the atomic number and E_c is the cutoff value for protons. E_c has been taken to be a free parameter to be determined from a comparison of the observed MMD with expectations from simulations. We carried out simple simulations to study the sensitivity of the MMD for various observable parameters, for example, primary energy including fluctuations, shower size at the observational level, number of shower particles summed over the unshielded detectors, etc.

A. Simulation procedure

The following basic assumptions underlie the simulations.

(a) The flux of all the five nuclear groups is taken to be known [33] at a total energy of 1 TeV/nucleus from direct measurements as mentioned above. Two models for the primary composition over the energy range of interest (10^{13}–10^{16} eV) were considered here for comparison, the constant mass composition (CMC) model and the low energy composition (LEC) model. The differential energy spectrum for each of the nuclear groups is represented by a power law,

$$\frac{dN}{dE}=K_i\times E^{-\gamma_i}, \tag{2}$$

where K_i and γ_i are from data [33] at 1 TeV for the ith nuclear group. The values of K_i are shown in the third column of Table I. In the CMC model, all five nuclear groups are assumed to have the same power law exponent of 2.7 from 1 TeV/nucleus onward until the cutoff energy value, $Z/A\times E_c$. The LEC model is characterized by different spectral exponents (fourth column in Table I) for the five nuclear components [33]. However, the knee in the LEC model is implemented in the same manner as in the CMC model.

(b) A large number of showers have been simulated for each nuclear group by randomly picking zenith angles be-

TABLE I. Spectral parameters from direct measurements.

Nuclear Group i	$\overline{A_i}$	Flux constant $(K_i \pm \sigma_{K_i})$ $(\mathrm{cm}^{-2}\ \mathrm{s}^{-1}\ \mathrm{sr}^{-1})$	Spectral slope $(\gamma_i \pm \sigma_{\gamma_i})$
Proton	1	0.1057 ± 0.003	2.76 ± 0.02
Helium	4	0.0673 ± 0.002	2.63 ± 0.02
CNO	14	0.0286 ± 0.004	2.67 ± 0.02
Silicon	28	0.0382 ± 0.002	2.66 ± 0.03
Iron	56	0.0236 ± 0.001	2.60 ± 0.04

tween 0° and 45° for the primary nuclei from an isotropic distribution at the top of the atmosphere but correcting for the projection of the detector plane to be normal to the axis of the shower. The energies of primary nuclei are sampled from the energy spectrum for the specific nuclear group, as per the composition model under consideration.

(c) The expected electron size (N_e) and muon size (N_μ) for each shower are picked from a large bank of simulated showers along with the shower age (s). This bank was generated using the COSMOS shower generator [34] for several energy and angle bins, for each of the five primary nuclear groups. It may be mentioned here that the COSMOS generator has been used very successfully to interpret observations on γ-ray families with emulsion chambers exposed at various high altitude stations (Mt. Fuji, Mt. Kanbala, and Mt. Chacaltaya). This generator is essentially based on parametrization of accelerator data, particularly the UA5 observations. Although CORSIKA [35] has become a very popular generator for simulation of air showers in recent years, particularly due to its wide adaptability for the use of several interaction models, it is well known [36] that most of the generators, using various interaction models, give similar, within about $\pm 10\%$, results at energies below $\sim 10^{15}$ eV. This is essentially due to the fact that the extrapolation for the energy dependence of various interaction parameters is relatively small and all the generators have been tuned to produce similar results at TeV energies. Therefore it has been suggested [36] that most of the results on air showers at energies below the knee for bulk properties such as electrons and low energy muons and hadrons need not be concerned about the differences among the interaction models, which become quite serious only at much higher ($\geqslant 10^{17}$ eV) energies.

Using the large number of showers in the bank, it was observed that the shapes of the distributions of $N_e/\overline{N_e}$ as well as $N_\mu/\overline{N_\mu}$ are essentially independent of the primary energy, for a given angle bin ($\sec\theta$) and a primary particle type. Therefore a much larger bank of showers can be obtained by combining showers of different primary energy groups but the same angle bin and primary particle type after converting the N_e and N_μ values for each shower to the corresponding ratios $N_e/\overline{N_e}$ and $N_\mu/\overline{N_\mu}$, where the average values $\overline{N_e}$ and $\overline{N_\mu}$ were computed separately for each energy group. Simulations have also been used to obtain the relations between the average electron size $\overline{N_e}$, average muon size $\overline{N_\mu}$, primary energy E_o, and zenith angle (θ). For example, these relations for primary protons (E_o in TeV) are as follows:

$$\overline{N_e} = 2.06 \times 10^2 E_o^{1.099} (2.56 \times \cos\theta - 1.547), \tag{3}$$

$$\overline{N_\mu} = 2.48 \times 10 E_o^{0.824} (0.823 - 1.099 \times \cos\theta + 2.833 \times \cos^2\theta - 1.555 \times \cos^3\theta). \tag{4}$$

The average electron size, muon size, and age are computed [32] for the primary energy and zenith angle, using relations appropriate for the primary particle type. A shower is then picked randomly from the appropriate bank for the specific particle type and angle bin. The fractional values $N_e/\overline{N_e}$, $N_\mu/\overline{N_\mu}$, and $s/\overline{s}$ stored for this shower are then converted to N_e, N_μ, and s as appropriate. As may be expected, this procedure retains all the fluctuations that occur in the development of an individual shower and the correlations between N_e, N_μ, and s for this shower as if it was generated through a full-fledged simulation procedure. The biggest limitation of this semi Monte Carlo simulation procedure is the extent of rare fluctuations as their frequency is essentially limited by the size ($\sim 10\,000$) of the shower bank available for each angle bin and primary particle type. However, this limitation is expected to have no detectable effect on the results in practice since we are looking at the bulk properties of the electron and muon components and not searching for very rare processes.

(d) As discussed in detail in Sec. II C, in the GRAPES-2 experiment the EASs have been selected using a fourfold coincidence between the signals from the four scintillators N, E, W, and S located near the center of the array (Fig. 1). Therefore shower selection is not uniform over the entire area of the array. In particular, small size EASs, which form the bulk of the data, have their cores preferentially closer to the center of the array, with nearly 80% of the observed showers having their core within 15 m of the center. Therefore, during the simulations also, the coordinates (X_o and Y_o) for the cores of showers were selected randomly over the central area of 15 m radius around the center of the array. Given these basic parameters E_o, A, θ, ϕ, X_o, Y_o, N_e, N_μ, and s for a simulated shower, it is straightforward to calculate the expected average electron density for each of the shower detectors, including the selection detectors N, E, W, and S, using the lateral density distribution as given by the Nishimura-Kamata-Greisen (NKG) relation:

$$\Delta_e^i = \frac{2\pi R_e^2 N_e}{\Gamma(2-s)\Gamma(4.5-s)} \left(\frac{r_e^i}{R_e}\right)^{(s-2)} \left(1 + \frac{r^i}{R_e}\right)^{(s-4.5)}, \tag{5}$$

where Δ_i is the average particle density over the ith detector located at a distance r_i from the shower core. The NKG parametrization is known to provide a good fit to the lateral distribution of shower particles over a broad shower size range, particularly for core distances shorter than the Molière radius ($R_e = 80$ m at Ooty).

(e) These values of average particle densities are then used for calculating the observed number of particles (n_e^i) by including Poisson fluctuations. Using the numbers so obtained for the selection detectors, it is determined whether the specified selection conditions are satisfied. Using this procedure and a very large number of such simulated showers, the values of the shower trigger efficiency (N_{sel}/N_o) were determined for various primary energy and zenith angle bins for each of the five primary particle types. Here, N_{sel} is the number of showers satisfying selection conditions out of a total of N_o showers simulated. The expected number of particles for each shower detector has also been determined using the average particle density at each detector. These numbers are used to obtain the particle sum $N_e^{psum}=\Sigma^i n_e^i$ over a selected number of shower detectors.

(f) For each simulated shower satisfying the selection criteria, the expected average muon density is computed for the position of each of the 192 muon detector modules using the value of N_μ obtained as described in (d) above and the muon lateral distribution parametrized by Greisen [37] as follows:

$$\Delta_\mu^j=\frac{\Gamma(2.5)}{2\pi\Gamma(1.5)\Gamma(1.5)}\left(\frac{1}{320}\right)^{1.25}N_\mu r_j^{-0.75}\left(1+\frac{r_j}{320}\right)^{-2.5}. \tag{6}$$

Here r_j is the distance of the jth muon detector module from the shower core. The expected number of muons incident over each module is then obtained by including the Poisson fluctuations and the muon triggering efficiency (Sec. II B). Counting the number of modules triggered, the observable N_μ^{mod} is determined for each shower.

With the above procedure, we have the following information available for each simulated shower which has satisfied the shower selection criteria: primary energy, particle type, zenith angle, shower size, particle densities at all shower detectors, particle sum N_e^{psum} over a selected number of shower detectors, and number N_μ^{mod} of muon modules triggered. Note that the value of the shower trigger efficiency determined above from simulations, combined with the value of the expected flux (Table I) for a particular nuclear group, yields the expected rate of showers, which can be compared with the observed shower rate.

B. Simulation results

We studied the shape of the MMD as a function of various shower observables to get some insight into the development of showers in the atmosphere and to assess the sensitivity of these observables to the composition of the primary flux. There is a basic difference in energetics between showers initiated by protons and other nuclei (A) of the same primary energy (E_o). In the simple superposition model of the development of showers initiated by nuclei, the shower is considered to be a superposition of A showers, each initiated by a nucleon of energy (E_o/A). Studies [38] have shown from a comparison of the results obtained using the superposition model with models incorporating more realistic break-up of nuclei in the upper atmosphere that the characteristics of most of the observables, such as the number of electrons, low energy ($\sim$1 GeV) muons and hadrons, and Cherenkov photons, are very similar. However, the number of low energy muons is significantly larger for a nuclear-initiated shower due to the production of a larger number of lower energy secondary pions in the upper and middle atmosphere and a larger probability of their decay to muons. This feature can be seen clearly from Fig. 9, which shows the expected distribution of the number of triggered muon detector modules for showers of fixed energy of 700 TeV. Note that these distributions have been generated following the full simulation procedure outlined in Sec. III A above, including satisfaction of the shower selection criteria. The mean muon multiplicity, computed from the five distributions shown in Fig. 9, plotted against the atomic mass A in Fig. 10, shows a simple power law relation $\overline{N}_\mu^{mod}=\mu_0 A^\gamma$. The values of the parameters μ_0 and γ are listed in the first row of Table II along with the shower observable. It is to be noted that the value of $\overline{N}_\mu^{mod}$ for Fe-initiated showers is almost twice the value for proton-initiated showers.

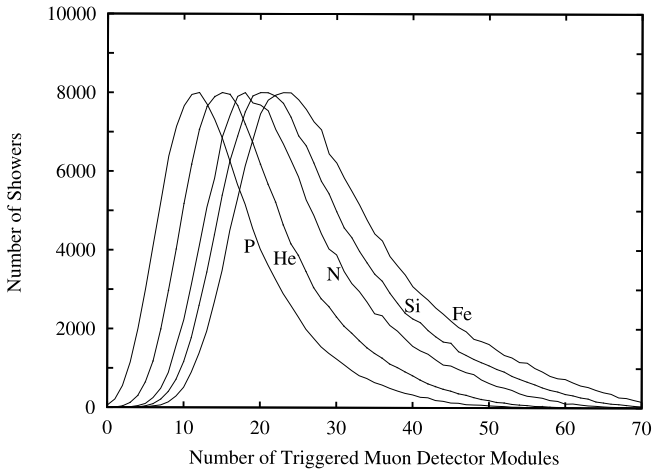

FIG. 9. Expected muon multiplicity distributions for showers initiated by different primary nuclei for fixed primary energy of 700 TeV, but normalized to the same peak value.

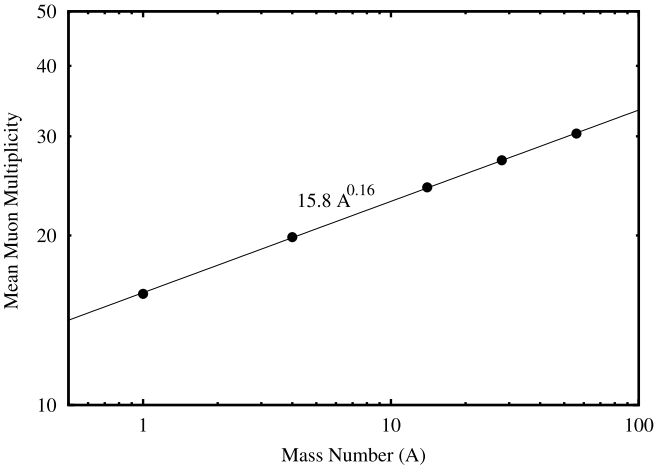

FIG. 10. Relation between the expected mean muon multiplicity and the atomic mass of primary nuclei for showers of fixed primary energy of 700 TeV.

TABLE II. Values of the fit parameters, μ_0 and γ for the relation $\overline{N}_\mu^{mod} = \mu_0 A^\gamma$.

Shower observable	Observable range	Constant (μ_0)	Slope (γ)
Primary Energy (fixed)	700 TeV	15.6	0.16
Primary Energy (bin)	500-1000 TeV	15.2	0.16
Shower Size (Ne)	$10^5 - 2\times10^5$	12.4	0.24
Particle Sum ($\Sigma\,\Delta_i$)	100-200	5.5	0.32

It may be seen from Fig. 9 that the distributions are rather broad even though they are for showers of a fixed energy with their cores incident over a restricted range of distances from the muon detector. The distributions obtained for primary energies spread over the energy interval 500–1000 TeV, using energy spectra given in Table I, have been found to be almost identical to those for a fixed primary energy of 700 TeV. This shows that most of the width of the distributions is contributed by the fluctuations in shower development. Similarly, the dependence of $\overline{N}_\mu^{mod}$ on the atomic mass for 500–1000 TeV showers is also nearly identical (second row of Table II) to that shown in Fig. 10 for showers of fixed energy of 700 TeV. Note that the distributions shown in Fig. 9 have been plotted after normalizing them to the common peak value, to highlight the differences due to the atomic mass. However, in reality, the number of showers expected for different nuclear groups is quite different, due to the large differences between their energy spectra (Table I). Figure 11 shows the distributions normalized to the expected flux values. Figure 11 also shows the distribution expected for the experimentally observable quantity, the ''sum'' of the five distributions. Note that the sum distribution is dominated essentially by the contributions due to showers initiated by lighter nuclei (p+He) in the 0–30 region and heavier nuclear groups (Si+Fe) for $\overline{N}_\mu^{mod} \geqslant 40$.

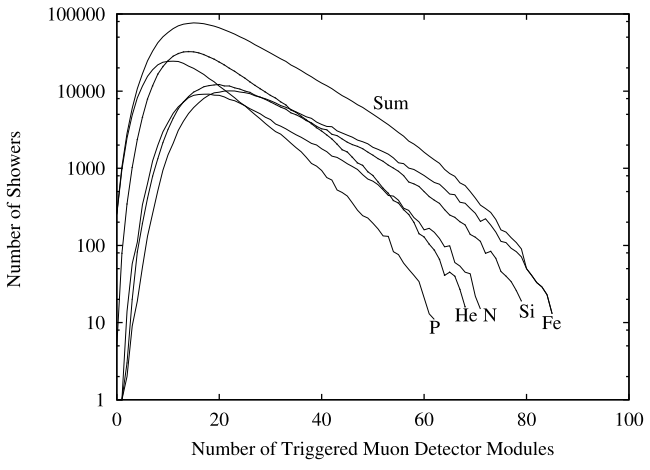

FIG. 11. Expected muon multiplicity distributions for showers initiated by different primary nuclei for primaries spread over the interval 500–1000 TeV, using the energy spectra given in Table I. Distribution marked ''Sum'' represents the observable distribution, which is the sum of the distributions for the five nuclear groups.

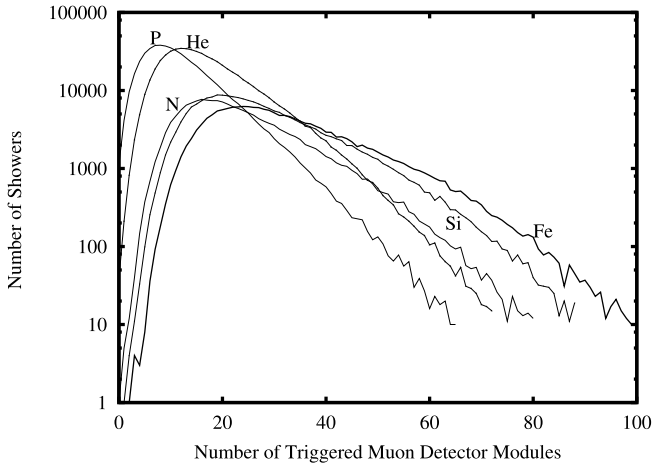

FIG. 12. Expected muon multiplicity distributions for showers initiated by different primary nuclei for the size range 10^5–2×10^5, using the energy spectra given in Table I.

A commonly used observable for estimating the shower energy is the shower size, which is obtained by integrating the lateral distribution function [Eq. (5)] over the densities of charged particles observed in unshielded detectors of the shower array. However, the shower size is subject to large fluctuations, primarily due to fluctuation in the atmospheric level of the first interaction of the primary particle, especially protons. Figure 12 shows the expected distributions for showers initiated by the five nuclear groups for the shower size range 10^5–2×10^5, normalized for relative flux values (Table I). However, no spectral steepening has been assumed to account for the knee in the spectrum for this set of simulations. Once again, the relation between $\overline{N}_\mu^{mod}$ and A can be nicely fitted by a power law. The parameters of the fit are listed in the third row of Table II. Note that the slope value, 0.24, is significantly larger now compared to showers with energy in a fixed range. This is as expected since showers initiated by heavier nuclei are required to have larger primary energy to give the same observable size due to their faster development in the atmosphere. Also note that the distributions are slightly broader now than those shown in Fig. 11, as the energy range required is broader due to the selection over the size range 10^5–2×10^5. Quantitatively, the muon number at which the heavier nuclear groups (Si+Fe) start dominating over the lighter nuclei (p+He) has increased to 29 from a value of 27 for the showers shown in Fig. 11.

It may be noted that the energy spectra [33] shown in Table I are relatively flatter for all groups than those for protons. Therefore, we have also obtained muon multiplicity distributions for the constant mass model, assuming the same spectral index of 2.7 for all nuclear groups. These are shown in Fig. 13. Comparing these distributions with those shown in Fig. 12, it is easily seen that the contribution due to He is significantly reduced while the muon multiplicity at which the heavier nuclei (Si+Fe) start dominating has changed from 29 to 32.

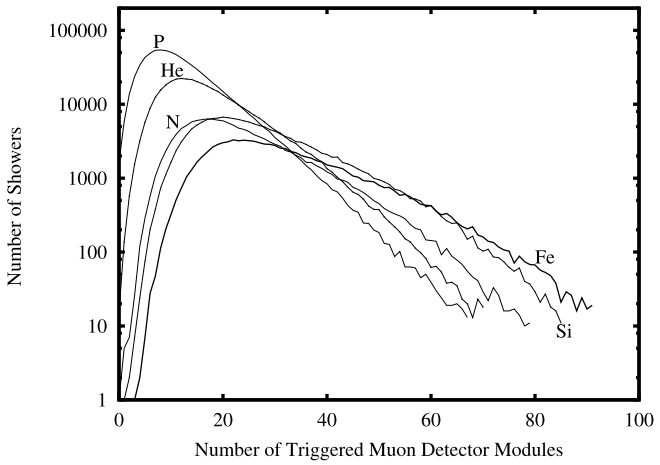

FIG. 13. Expected muon multiplicity distributions for showers initiated by different primary nuclei for the size range 10^5–2×10^5, using spectral constants as given in Table I but assuming a constant spectral index of 2.7 for all nuclear groups.

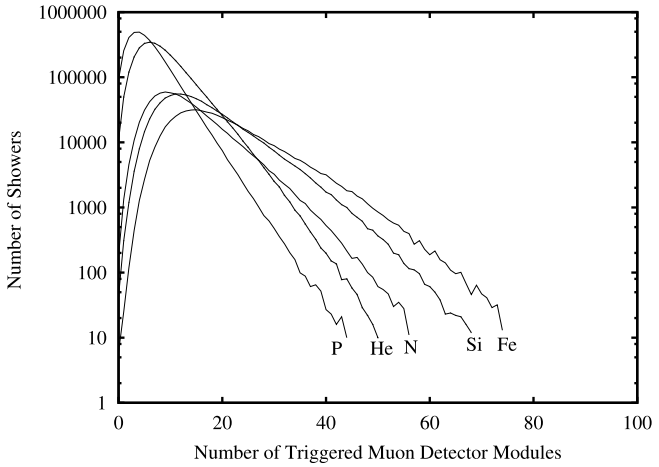

FIG. 14. Expected muon multiplicity distributions for showers initiated by different primary nuclei for the P_{sum} range 100–200 MIPS, using the energy spectra given in Table I.

It is well known that the measurement of shower size is subject to large errors if the shower array has a small number of detectors and/or the array size is small. This is due to the larger error in the determination of the shower age parameter for individual showers in such cases. Therefore it is suggested that the use of the parameter ''particle sum'' may be considered in place of shower size, particularly for smaller size showers. Of course, it is necessary to locate the shower core, using the center-of-gravity method, before calculating the particle sum (P_{sum}) over a well-defined number of detectors around the position of the shower core. Keeping the shower cores restricted to an area of radius 15 m around the array center for simulations as discussed above, we have also studied the muon distributions for various values of P_{sum} obtained from a sum over the number of particles (MIPS) expected in detectors located within the four inner rings (Fig. 1), i.e., the inner 37 detectors. Figure 14 shows the distributions expected for showers with P_{sum} in the range 100–200 MIPS, using the energy spectra given in Table I. The relation between $\bar{N}_{\mu}^{mod}$ and A is again well fitted by a power law, and the parameters are listed in the fourth row of Table II. It may be noted that, due to the relatively smaller size of showers selected with P_{sum} in the range 100–200 MIPS, which would have relatively flatter lateral distributions, P_{sum} seems to be more sensitive to the atomic mass as compared to the shower size N_e. This feature may also be seen from Fig. 14, since the muon multiplicity at which the heavier nuclei (Si +Fe) start dominating the light nuclei (p+He) has been significantly reduced to 16.

IV. OBSERVATIONS AND DISCUSSION

The hardware requirements for the shower trigger, discussed in detail in Sec. II C, consist of (a) a fourfold coincidence between signals at the $\gtrsim$0.3 MIP level from detectors N, E, W, and S and (b) a signal at the $\gtrsim$3 MIP level from any one of these four detectors. The observed trigger rate was 5.9 per minute. However, due to small changes in the gains of the PMTs of trigger detectors with time and suitable corrective readjustments, the trigger levels varied with time, resulting in some variation in the overall trigger rate. In order to avoid the effects of these variations on the results, it was decided during data analysis to impose software selection conditions which required (a) a fourfold coincidence between signals at the $\gtrsim$1.0 MIP level from detectors N, E, W, and S and (b) a signal at the $\gtrsim$6 MIP level from any one of these four detectors. The shower rate obtained from data collected over a period of 6 months (1.75×10^7 s) using these conditions was 3.6 per minute. It is interesting to study the distribution of triggered muon detector modules for showers satisfying these basic software trigger conditions. This distribution is shown in Fig. 15 using only 172 of the 192 modules of the muon detector.

Figure 15 also shows the expected distribution for protons with an assumed spectral index of 2.7. The expected distribution has been normalized to the total number of observed

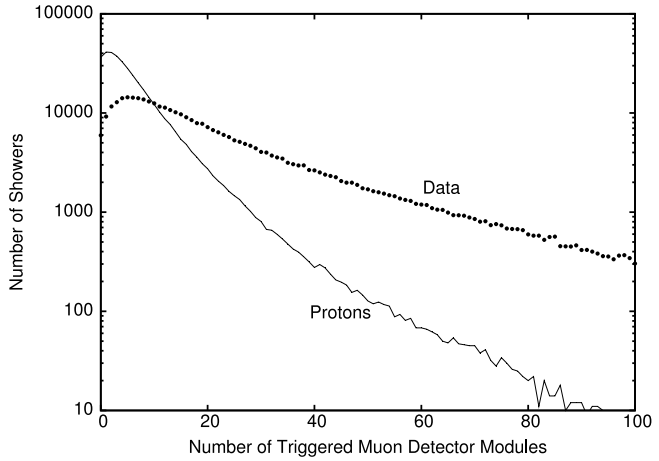

FIG. 15. A comparison of the observed muon multiplicity distribution for showers satisfying software selection conditions with the distribution expected for the same number of simulated proton showers ($\gamma_p=2.7$).

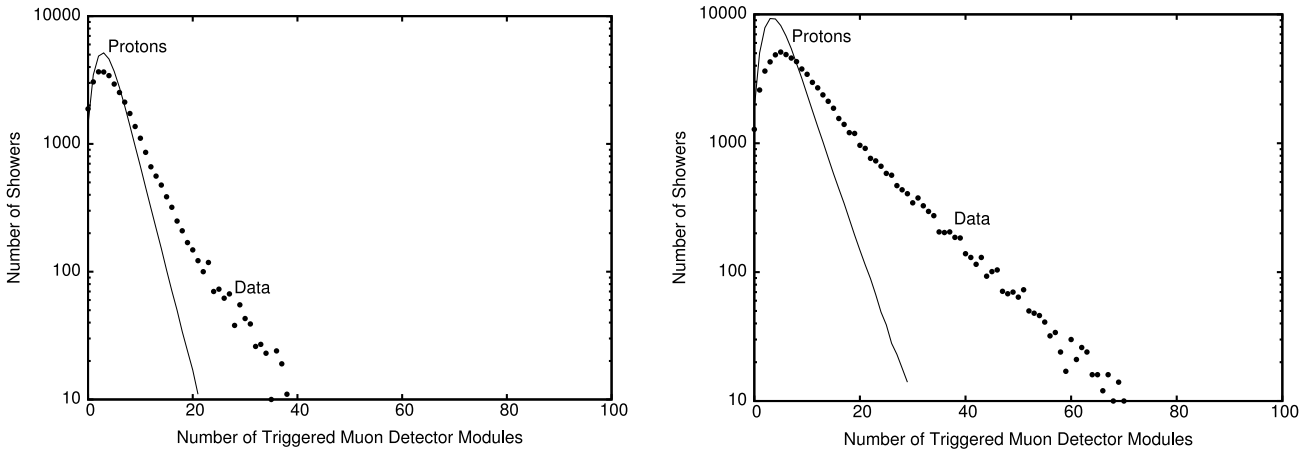

FIG. 16. A comparison of the observed muon multiplicity distribution for showers satisfying 'software' selection conditions with the distribution expected for equivalent number of simulated proton showers. The figure at left for P_{sum} range, 50–100 and at right for 100–200 particles respectively.

showers. It is to be noted that the expected number of showers is significantly larger than the number observed in the small muon number ($N_\mu^{mod} \lesssim 20$) region. However, there is a deficiency of showers in the larger number ($N_\mu^{mod} \gtrsim 30$) region compared to observations. Since there is no restriction on the core position for the observed showers used for the distribution shown in Fig. 15, the cores of simulated showers were also allowed to fall randomly over a large area (200 m radius) around the array center before imposing the selection conditions.

As discussed earlier in Sec. III B, the smaller and the larger muon multiplicity regions are relatively more sensitive to the number of lighter ($p+\mathrm{He}$) and heavier (Si+Fe) nuclei in the primary flux, respectively. Therefore, in principle, a suitable composition model can be found to give a satisfactory agreement between the observed and expected distributions by varying the spectral index γ_i for the five nuclear groups. Obviously, it is not advisable to vary the normalization constants K_i (Table I), in order to keep the compatibility of the derived spectral parameters with direct observations at lower energies ~ 1 TeV. Basically, there are 15 parameters whose variation can be considered to a limited extent around their nominal values, namely, the five spectral indices for the five nuclear groups from ~ 1 TeV up to the respective five energy cutoff values E_i^c, and the five spectral indices above the energy cutoff values. Note that any combination of these parameters must give an acceptable agreement with the expected all-particle spectrum as determined from direct observations up to $\sim 10^{15}$ eV as well as the energy spectrum derived from observations of the shower size spectrum at energies $\gtrsim 10^{15}$ eV. The exercise of finding a suitable composition model to fit the observed distribution shown in Fig. 15 is in progress, and its results will be reported in a future publication.

As suggested in the previous section, we have also looked at data with P_{sum} as a measure of the shower size (N_e) for small size showers, in order to avoid large errors in the determination of N_e. Simulations have shown large sensitivity of the muon multiplicity distribution for the P_{sum} range 100–200 for the GRAPES-2 array. Figure 16 compares the observed distributions for two ranges of P_{sum}, 50–100 MIPS (left) and 100–200 MIPS (right) with the results from simulations for proton-initiated showers that satisfy the software selection conditions. It is interesting to note that, while both the observed distributions have many more showers with a large number of triggered modules, the difference between the observed and expected distributions is much more prominent for showers with larger P_{sum}. This feature is not surprising since showers with smaller values of P_{sum} have smaller triggering efficiency. Simulations show that the triggering efficiency becomes close to unity only for P_{sum} values $\gtrsim 500$ for the selection conditions used in the present analysis. It is well known that only showers initiated by protons are able to satisfy the selection conditions very close to the threshold, and the contributions due to heavier nuclei start coming in only at higher energies. Therefore it is expected that the observed muon multiplicity distribution will be closer to the distribution for proton showers near the triggering threshold. On the other hand, the presence of showers with larger values of $\overline{N}_\mu^{mod}$, compared to proton showers, shows clearly the contribution of showers due to heavier nuclei. However, as mentioned above, extensive simulations are required to find a composition model that would yield a good agreement between the observations and expectations. This work is also in progress.

For the present, the main result obtained from the comparison of observed muon multiplicity distributions with simulations, Figs. 15 and 16, is that a composition heavily dominated by lighter nuclei is not favored. Following the results shown in Figs. 12, 13, and 14, it is clear that a significant amount of heavier nuclei is required to understand the tail in the observed multiplicity distributions. This qualitative conclusion is consistent with the results obtained from other experiments [10–13], where correlations between electrons and low energy muons were studied using large area muon detectors. However, there are large discrepancies among the results obtained using different components [3,39] of the air showers. The discussion above also brings out the

fact that a simultaneous fit to the smaller and larger number regions of the muon multiplicity distribution has the potential to determine the contributions due to lighter and heavier nuclei to the cosmic ray flux in the energy region 10^{14}–10^{15} eV almost independently.

V. SUMMARY

The salient features of the experimental system of the GRAPES-2 experiment relevant for observations of the muon multiplicity distribution have been described in some detail. The results from the simulations presented above have highlighted the sensitivity of the number of muons observed with a large area detector for showers with well-defined characteristics of the electron component to the atomic mass of primary nuclei. A few observations have been presented on the muon multiplicity distributions for different selection conditions on the electron component and compared with the expectations from simulations. These clearly show the need to include the contribution of heavy nuclei in the primary flux, relatively independently of the assumptions about the primary proton energy spectrum. Detailed simulation work is in progress to deduce results on the primary composition from observations around energies $\sim 10^{15}$ eV.

ACKNOWLEDGMENTS

It is a pleasure to thank the engineers B. Jasper, G. A. Kumar, A. V. Panse, R. Rajagopal, and B. S. Rao for their contributions to the development of the electronics and the software for the data acquisition system and the civil infrastructure for the detectors. The technical help given by A. A. Basha, D. B. Arjunan, G. P. Francis, I. M. Haroon, V. Jeyakumar, R. Nisha, K. Ramadass, C. Ravindran, and V. Viswanathan for the day-to-day maintenance and operation of the experimental system and the laboratory at Ooty is thankfully acknowledged.

[1] V.S. Berezinskii *et al.*, *Astrophysics of Cosmic Rays* (North-Holland, Amsterdam, 1990).
[2] P.L. Biermann, J. Phys. G **23**, 1 (1997); B. Wiebel-Sooth *et al.*, Astron. Astrophys. **330**, 389 (1998).
[3] P. Sommers, invited talk, Rapporteur and Highlight Papers, 27th ICRC, Hamburg, 2001, p. 170.
[4] R. Ong, Phys. Rep. **305**, 93 (1998).
[5] E. Lorenz, J. Phys. G **27**, 1675 (2001).
[6] K. Asakimori *et al.*, Astrophys. J. **502**, 278 (1998).
[7] A.V. Apanasenko *et al.*, Astropart. Phys. **16**, 13 (2001).
[8] A.W. Wolfendale, J. Phys. G **29**, 787 (2003).
[9] M.V.S. Rao and B.V. Sreekantan, *Extensive Air Showers* (World Scientific, Singapore, 1998), p. 165.
[10] M. Aglietta *et al.*, in Proceedings of the 26th ICRC, Salt Lake City, Utah, 1999, Vol. 1, p. 230.
[11] M.A.K. Glasmacher *et al.*, in Proceedings of the 26th ICRC, Salt Lake City, Utah, 1999, Vol. 1, p. 129; M.A.K. Glasmacher *et al.*, Astropart. Phys. **12**, 1 (1999).
[12] K.-H. Kampert, in Proceedings of the 26th ICRC, Salt Lake City, Utah, 1999, Vol. 3, p. 159; K.-H. Kampert, invited talk, Rapporteur and Highlight Papers, in Proceedings of the 27th ICRC, Hamburg, 2001, p. 240; T. Antoni *et al.*, Astropart. Phys. **16**, 245 (2002).
[13] V.S. Eganov *et al.*, in Proceedings of the 27th ICRC, Hamburg, 2001, p. 222; J. Phys. G **26**, 1355 (2000).
[14] S.C. Tonwar, Bull. Astron. Soc. Ind. **30**, 147 (2002).
[15] Y. Hayashi *et al.*, in Proceedings of the 27th ICRC, Hamburg, 2001, p. 111.
[16] S. Ahlen *et al.*, Phys. Rev. D **46**, 895 (1992); M. Ambrosio *et al.*, *ibid.* **56**, 1418 (1997).
[17] S.M. Kasahara *et al.*, Phys. Rev. D **55**, 5282 (1997).
[18] H.R. Adarkar *et al.*, Phys. Rev. D **57**, 2653 (1998).
[19] V.N. Bakatanov *et al.*, Astropart. Phys. **12**, 19 (1999).
[20] J. Ridky and P. Travnicek, Report No. DELPHI 2002-075-CONF-609, 2002.
[21] V. Avati *et al.*, Astropart. Phys. **19**, 513 (2003).
[22] M. Aglietta *et al.*, Phys. Lett. B **337**, 376 (1994); G. Navarra, in Proceedings of the 27th ICRC, Hamburg, 2001, p. 120.
[23] M. Aglietta *et al.*, Astropart. Phys. **9**, 185 (1998).
[24] H. Wilkens, in Proceedings of the 27th ICRC, Hamburg, 2001, p. 605, Ph.D. thesis, University of Nijmegen, 2003.
[25] S.C. Tonwar *et al.*, Astrophys. J. Lett. **330**, L107 (1988).
[26] S.K. Gupta *et al.*, Astrophys. J. Lett. **354**, L13 (1990).
[27] S.C. Tonwar *et al.*, Phys. Rev. Lett. **67**, 2248 (1991).
[28] S.C. Tonwar *et al.*, Astrophys. J. **390**, 273 (1992).
[29] S.K. Gupta *et al.*, Phys. Rev. D **48**, 3463 (1993).
[30] S.K. Gupta and T.S. Selvakumaran, TIFR-HECR-CRL Technical Note No. 01/88, 1988.
[31] B.B. Snavely *et al.*, Appl. Phys. Lett. **11**, 275 (1967).
[32] R. Srivatsan, Ph.D. thesis, Bombay University, 1994.
[33] B. Wiebel-Sooth and P. Biermann, in *Numerical Data and Functional Relationships in Science and Technology*, edited by H.H. Voigt, Landolt-Börnstein, New Series, Group VI, Vol. 3, part c (Springer-Verlag, Berlin, 1999), pp. 37–90.
[34] K. Kasahara and S. Torii, Comput. Phys. Commun. **64**, 109 (1991); K. Kasahara, in Proceedings of the 24th ICRC, Rome, 1995, Vol. 1, p. 309; M. Amenomori *et al.*, in Proceedings of the 27th ICRC, Hamburg, 2001, p. 2395; COSMOS webpage, http://eweb.b6.kanagawa-u.ac.jp/kasahara/ResearchHome/COSMOSHome/index.html
[35] D. Heck *et al.*, in Proceedings of the 27th ICRC, Hamburg, 2001, p. 233; Report No. FZKA 6019, Forschungszentrum Karlsruhe, 1998.
[36] S.C. Tonwar, in *Proceedings of the 12th ISVHECRI*, Geneva, Switzerland, 2002 [Nucl. Phys. B (Proc. Suppl.) (in press)].
[37] K. Greisen, Annu. Rev. Nucl. Sci. **10**, 63 (1960).
[38] T.K. Gaisser *et al.*, Rev. Mod. Phys. **50**, 859 (1978).
[39] J.R. Horandel, Astropart. Phys. **19**, 193 (2003).